CEAS Aeronautical Journal
https://doi.org/10.1007/s13272-025-00922-2

ORIGINAL PAPER

High-pressure testing of hydrogen fuel injectors in a triple-sector RQL-rig for the Rolls-Royce Pearl 15 Hydrogen Demonstrator Engine Program

Sebastián Eisenring[1] · Thomas Behrendt[1] · Johannes Berger[1] · Peter Tiessen[1] · Bertram Janus[1] · Carsten Clemen[2]

Received: 2 June 2025 / Revised: 22 August 2025 / Accepted: 27 October 2025

Abstract

As part of Germany's LuFo 6 program 'WOTAN', Rolls-Royce Deutschland (RRD) investigated direct H_2 combustion in Rich-Quench-Lean (RQL) mode. Two H_2-injectors, previously tested under atmospheric conditions, were evaluated at elevated pressures and preheat temperatures in the High-pressure Optical Triple Sector (HOTS) at DLR's HBK1 facility. These tests served as a safety check for the following full-annular test at take-off operating condition. Both injectors were tested at 7% take-off load, with variations in air-to-fuel ratio (AFR) to examine the effects of stoichiometry on flame characteristics and NO_x emissions. Flame imaging was conducted using ultra-violet (UV)-, near-infrared (NIR)-, and visible spectrum diagnostics to visualize OH*, water vapor and flame luminosity. Exhaust gas measurements were performed downstream of the combustion chamber's convergent section. Both injectors demonstrated stable combustion across all test conditions, maintaining consistent flame position and shape despite changes in pressure, temperature and AFR. However, significant differences in NO_x emission index (EI) were observed between the injectors. The injector with higher NO_x emissions exhibited flame anchoring at the injector exit, while the other maintained a lifted flame, reducing thermal NO_x formation. Additionally, AFR variation revealed different sensitivities of EI NO_x, attributed to distinct fuel placement and local stoichiometry. One injector developed a second heat release zone in the inner recirculation region at higher AFRs, further contributing to elevated NO_x.

Keywords H_2 direct combustion · RQL-combustion · H_2O-imaging · OH*-chemiluminescence · NO_x

1 Introduction

In an effort to reduce green house gas (GHG) emissions stemming from air travel, hydrogen combustion has been chosen by the German Ministry of Economy and Climate Protection as one feasible pathway to be investigated. For reasons of competitiveness and rapid market entry of combustors burning hydrogen, retrofitting existing combustors optimized for kerosene combustion with new hydrogen injectors would be preferable. Yet, the widely different combustion characteristics of liquid kerosene and gaseous H_2 might lead to unwanted combustion related issues. At the same equivalence ratio, hydrogen exhibits higher flame temperatures and higher burning velocities than kerosene. Gaseous fuels, especially hydrogen, are mixed faster with air than liquid fuels, because no prior atomization and evaporation is necessary. Accordingly, the insertion of hydrogen injectors into combustors optimized for kerosene

✉ Sebastián Eisenring
sebastian.eisenring@dlr.de

Thomas Behrendt
thomas.behrendt@dlr.de

Johannes Berger
johannes.berger@dlr.de

Peter Tiessen
peter.tiessen@dlr.de

Bertram Janus
bertram.janus@dlr.de

Carsten Clemen
dr.carsten.clemen@rolls-royce.com

[1] Institute of Propulsion Technology, German Aerospace Center (DLR), Linder Höhe, 51147 Cologne, North Rhine-Westphalia, Germany

[2] Rolls-Royce Deutschland Ltd. & Co. KG, Eschenweg 11, 15827 Blankenfelde-Mahlow, Brandenburg, Germany

Published online: 11 November 2025

combustion could lead to combustion instabilities, excessive temperatures at the combustion chamber walls and at the turbine inlet and higher NO_x-emissions. Therefore, careful thought has to be put into the design of the injectors, especially regarding fuel placement and fuel-air mixing, so as to optimize the burning of H_2 with respect to combustion stability and NO_x.

Few experimental studies regarding hydrogen combustion under realistic operation in aviation application have been done so far. Kroniger [1] investigated the NO_x-emissions of a stationary gas turbine combustor at different hydrogen-natural gas blends at realistic operating conditions. More specifically he examined the influence of increasing hydrogen content in the fuel blend on the NO_x production. While application-oriented, the employed combustor did not have any optical access, impeding any observation of the possible changes to flame morphology by increasing hydrogen content. Giannouloudis [2] investigated micromix combustion in the context of aviation combustors using hydrogen as fuel at intermediate pressures. The NO_x was measured at different combustor pressures, temperatures and stoichiometries. While similar operating conditions were tested as in the here presented paper, again no optical accessability was possible during the experiments. Furthermore micromix technology is not yet employed in aviation, unlike the RQL-combustion technology in the presented study. While hydrogen combustion is a highly researched topic, few investigations show realistic hardware or operation as seen in aircraft. Results from optically accessible test rigs at intermediate pressures are similarly difficult to come by.

It is the purpose of the here presented investigation to expand on the research of hydrogen combustion in an application-oriented RQL-combustor with optical access and emission probing. For this purpose the Institute of Propulsion Technology of DLR works in close collaboration with Rolls-Royce Germany (RRD) in the LuFo VI program 'WOTAN'. The goal of this collaboration was to, first, design and test 5 hydrogen injectors at low TRL in the Atmospheric Primary Zone (APZ) test section and downselect 2 injectors for further testing at higher TRL. This campaign was conducted by Berger et al. [3]. The second step was the intermediate and high pressure tests in the HOTS-combustor in the HBK1 test rig. The here presented investigation focuses on the NO_x-emission characteristics of the downselected hydrogen injectors with respect to changing stoichiometry at idle engine condition in the application-oriented HOTS-combustor. Once the operation stability of the hydrogen injectors at engine part-loads in the HOTS was verified, another round of testing was done in the full-annular test section of HBK5 up to full engine load. The results of which are reported by Clemen et al. [4].

The main GHG and pollutants generated by conventional aircraft engines running on hydrocarbons are CO_2, NO_x, unburnt hydrocarbons (UHC), soot and water vapour. Replacement of hydrocarbons by hydrogen as fuel leaves only NO_x and water vapour as main contributors to pollutant emissions and positive radiative forcing (RF). The International Civil Aviation Organization (ICAO) has set ever more stringent NO_x-emission limits of aircraft engines over the past decades. NO_x-emission restrictions are focused on the harmful effect of NO_x on the ground air quality. Besides the detrimental effect on local air quality, NO_x-emissions at cruise altitudes also possess a net positive RF [5]. The extent of the RF of NO_x from aviation is still uncertain and discussed [6]. Consequently, the ICAO suggested to further tighten the NO_x-emission regulation for the Landing and Take-Off cycle and to develop a NO_x-emission metric for cruise conditions [7]. Considering that without CO_2 emissions, NO_x and water vapour would be the primary contributors to net RF of hydrogen combustion, the understanding of NO_x-formation in applied hydrogen flames receives a new urgency.

The formation of NO_x in non-premixed hydrogen flames is mainly described by the thermal NO reaction pathway. Thermal NO is favoured by burnt gas temperatures (T_b) typically above 1800K and requires oxygen. Conventional aircraft engine combustors burn the fuel-air-mixture in RQL mode. Figure 2 shows the main combustion zones in the HOTS test section. In the primary zone the combustion takes place in fuel-rich mode. This keeps the reaction rate of NO_x low since oxygen is scarce and T_b is low. The addition of large amounts of air in the mixing zone quickly mixes with the gas mixture resulting from incomplete combustion in the primary zone and transitions the mixture from fuel-rich to fuel-lean, evading the high temperature combustion near stoichiometry and finishing the reaction in the lean secondary zone. The residence time in regions with high NO_x production rates determines the total amount of NO_x present at the end of the combustor. Typically, high residence times are found in the inner and outer recirculation zones (IRZ and ORZ) of hot gases in the primary zone. Therefore, it is of paramount importance to reduce the formation rates of NO_x in those regions. The extent of fuel-air mixing at the reaction zone has strong effect on local T_b and thus NO_x production rates. Lyons et al. [8] found that NO_x-levels increase with increasing inhomogeneity of the fuel-air mixture of globally constant equivalence ratio at lean and rich combustion. At near-stoichiometry NO_x-emissions decrease with increasing fuel-air mixture non-uniformity. Both injectors in the herein presented investigation have separate fuel and air passages up until the exit of the injector. The quality of mixing of fuel and air and the flame stabilization will have a big impact on the NO_x-emissions of each injector. In summary, four

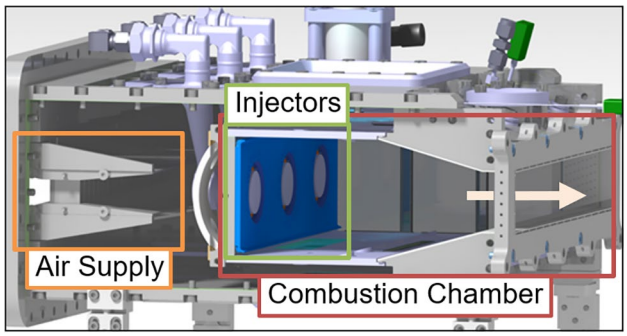

Fig. 1 Overview of the HOTS test section

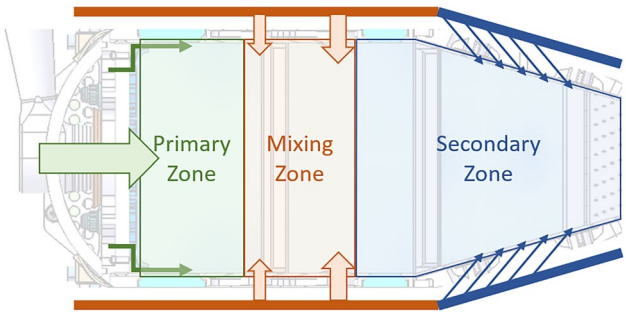

Fig. 2 The HOTS-combustion chamber, as seen perpendicular to the windows, with sketched air inlets (arrows) and combustion zones. Cross sectional view

important parameters, AFR, the residence time, the fuel-air mixing quality and the local O_2-concentration, determine the final NO_x-emissions in RQL-combustors.

The imaging of the flames with respect to their radiation in the UV- and NIR-radiation can give insights into the location of the heat release, using OH*-chemiluminescence as marker [9–11], and into the location of hot burnt gases, using the water vapour radiation in the NIR-spectrum as indicator. These insights into the flame shape, the progress of reaction and global flow phenomena are used to interpret the measured NO_x-emission differences of both injectors.

2 Test campaign and experimental setup

The aim of the campaign was to corroborate the observations made for two of five hydrogen injectors investigated under atmospheric conditions by Berger et al. [3] regarding their combustion stability and NO_x-emission behaviour at power ratings relevant to engine operation. In the following section the test campaign details, flame imaging setup and exhaust gas measurement is explained.

2.1 HOTS-combustor

The RRD-injectors were tested in the HOTS. The HOTS is operated with three identical injectors. The relative axial position of the injectors with respect to the heat shield can be varied. Preheated air reaches the combustor through a diffuser (see Fig. 1). The preheated air is distributed along the combustion chamber according to the air splits defined by the effective areas of the air inlets into the combustion chamber. Further details are explained by Meier et al. [12].

The HOTS is a combustor designed for RQL-combustion of kerosene. The HOTS is based on the development of the combustion chamber employed in the BR715-engine [13]. Figure 2 shows where the three combustion zones are located in the HOTS. Optical access of the entire combustor length and height is provided by quartz-windows. For this test campaign only the side facing the camera was lined with windows. The other side was closed with metal wall-elements. A metal separator downstream of a window applies a new cooling air film on the following windows. These separators partially obstruct the view of the cameras on the combustion, this limitation is explained further below.

2.2 RRD-H_2-injectors

The tested injectors are named V2 and V5 and are shown in Fig. 3. Figure 4 shows the individual flow passages through the injector exit. The central air flow of V2 is swirled and exits the injector through a diffuser. The fuel flow exits the

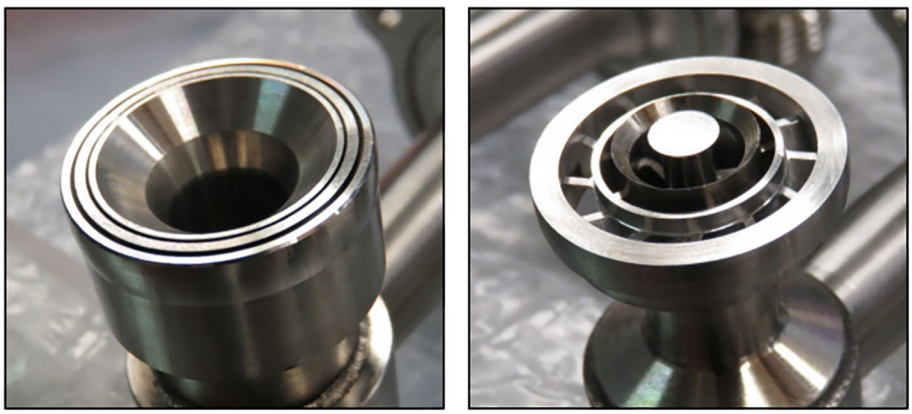

Fig. 3 Close-up of the investigated injectors. V2 on the left and V5 on the right

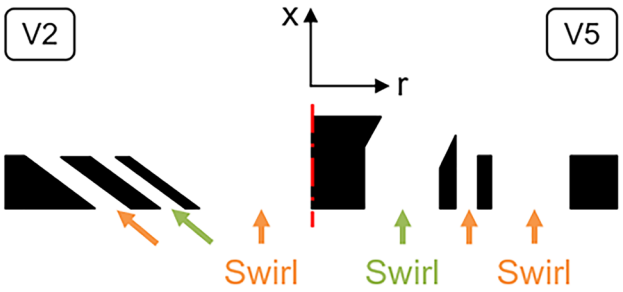

Fig. 4 Side-by-side comparison of a schematic sectional view through the exit of the injectors. Orange arrows denote the air flow and green arrows the fuel flow

injector at an angle, resulting in a radial and axial component of the velocity vector. The outer air flow exits the injector similarly to the fuel flow. Of great importance are the steps, due to the wall thickness, between inner air-, fuel- and outer air passage. Diffusor and swirl generator in the central passage create a recirculation zone at the center line downstream of the injector, which forms a stagnation point at the exit of the central air passage and deflects the air flow radially outwards. The outer air flow was introduced by RRD mainly to protect the 'long' injector seal used in the atmospheric test campaign.

The V5-injector geometry is radically different. The fuel flow is located around a bluff-body in the center. The bluff-body and swirling motion of the fuel flow create an IRZ dominated by the fuel flow, which is blocked from protruding into the fuel flow in the injector by the bluff-body. The central fuel placement creates a fuel-rich region in the center of the primary zone, which was sought after, to reduce T_b and thus NO_x-emissions. The inner air passage makes up a small part of the total air mass flow through the injector. It was conceived so that fuel cannot be entrained in low velocity regions at the injector exit. The outer air flow imparts an additional swirling motion to the primary zone further enhancing the IRZ.

The effective area of the air flow passages of V2 equals 63% of V5's. Because the injectors are compared in the same combustor, the air split of the combustion chamber is different for each injector. The primary zone AFR, including the air from injector, burner seal, heat shield and wall cooling, of V2 is 137% of V5's. Therefore, quicker depletion of the fuel flow is possible in the primary zone. The observed consequences are discussed in Sect. 3.

2.3 Investigated operating conditions

The test points (TP) are defined by the quantities P_{30}, T_{30}, dP_{inj} and AFR_{inj}. AFR_{inj} is defined as the ratio of the calculated injector air mass flow and the measured hydrogen mass flow. P_{30} and T_{30} are the measured static pressure and air temperature between diffuser and injectors. dP_{inj} is the static pressure difference across the injectors.

At 7% take-off power rating three different AFR_{inj} were investigated with regard to flame shape and NO_x-emissions. The reference AFR_{inj} corresponds to the nominal AFR_{inj} at 7% take-off power rating. One leaner and one richer AFR_{inj} were defined as 116% and 87% of the reference AFR_{inj}, respectively. All TPs were fuel-rich in absolute terms at the location of the injector. The observation and discussion of the AFR_{inj}-variation is the topic of Sect. 3. At each TP the exhaust gas composition, the OH*-chemiluminescence in the UV-spectrum and the H_2O-radiation in the NIR-spectrum were measured.

2.4 Exhaust gas analyzer and cameras

In the following subsections the applied measurement devices and data postprocessing steps are listed and explained.

2.4.1 NO_x-concentration measurement

NO_x-concentration was measured by sampling the exhaust gas downstream of the combustor. The sampling probe, valves and exhaust tubes bringing the exhaust gas to the analyzers are heated to 165°C to avoid condensation along the way to the exhaust gas measurement system. The exhaust gas was analyzed for O_2- and NO_x-concentration, which were measured dry. The exhaust gas was dried to avoid cross sensitivity and condensation in the NO_x-analyzer, due to the high water concentration in the exhaust gas. NO_x was measured using ECO Physics' CLD 700 EL ht device, which measures NO-concentration directly and NO_2 indirectly by reduction to NO. NO is measured through detection of chemiluminescence upon reduction with O_3. The sum of concentrations of NO and NO_2 forms the measured NO_x-concentration. The linearity deviation corresponds to $\leq$1% of the measurement range [14]. The measurement of NO_x is cross-sensitive towards H_2O and CO_2 molecules. H_2O is removed from the exhaust gas, as explained above, and CO_2 concentration is close to it's concentration in ambient air. Therefore no relevant cross sensitivity is expected using the dried exhaust gas. The measurement range was set to 100ppm. O_2 was measured with Sick Maihak's gas analyzer model S710 Oxor-P in the measurement range of 0 to 21 vol.%. The linearity deviation is $\leq$1% of the measurement range [15]. The measured raw NO_x-values were converted to EI with units grams of NO_x per kilograms of fuel. For this purpose the dry-measured NO_x-concentration had to be corrected for the water content in the exhaust gas. Water concentration can be calculated assuming complete consumption of fuel with excess of oxygen, then

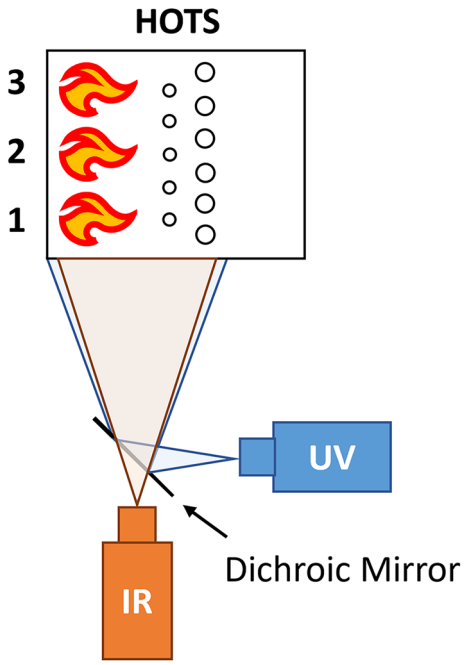

Fig. 5 Top-down view of the camera setup with respect to the HOTS

$[H_2O] = 2 * ([O_2]_{educts} - [O_2]_{products})$ holds. This condition is true at the sampling probe location.

2.4.2 Imaging of OH*-chemiluminescence and H_2O NIR-radiation

Chemically excited OH-radicals emit UV-radiation at a wavelength of 310nm. OH*-chemiluminescence of the flame was captured by a PCO Dicam Pro UV-camera with 1280x1024 pixel resolution and application of a 40% gain and 2x2 binning by the camera software. The camera had a 100 mm UV-lens and f/2.8. The OH*-signal from the flame was filtered using a bandpass-filter centered around a wavelength of 315nm with a bandwidth of 20nm. The exposure time was set to 55µs and 70µs for V2 and V5, respectively. At the same operating condition, the UV-signal of V2 was higher than that of V5, therefore the exposure time needed to be adjusted for each injector individually to maximize the signal-to-noise ratio. The same is true for the exposure time settings of the infrared camera explained below.

At sufficiently high temperatures H_2O-molecules emit NIR-radiation. Using the code by Rivière et al. [16] to calculate the spectral intensities of H_2O, it was found that the H_2O-signal in the observed spectral band increases linearly with the volumetric water vapour concentration in the flame and non-linearly with the local temperature. The radiation peak at a wavelength of 1425nm was chosen to capture the H_2O-signal. For this purpose a Xenics Xeva vSWIR infrared camera with a resolution of 320×256 pixel was used to image the water vapour in the combustion chamber. An

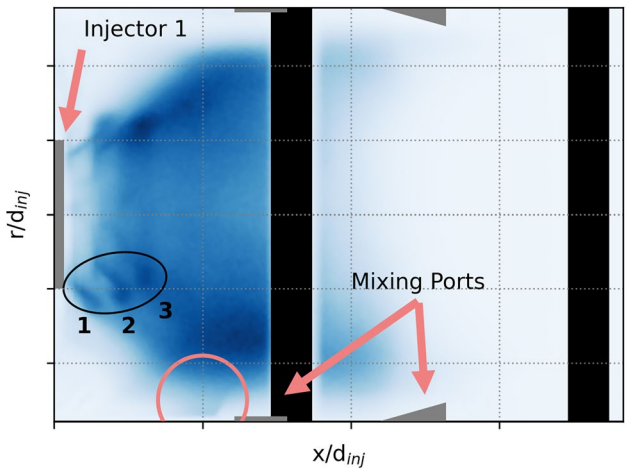

Fig. 6 LOS OH*-chemiluminescence of the V2-flame at TP06. The grey patches show the axial location of injector 1 exit and the first and second mixing row. The black columns show the location of the wall-elements described in Sect. 2.1. The numbers show the initial flame front of each injector. The circle shows UV-signal being reflected at the bottom of the combustor

OPTEC lens (P/N C1855) with 100 mm focal length and f/8 was mounted on the camera. Two filters were mounted on the lens: one bandpass-filter centered around a wavelength of 1425nm with a bandwidth of 190nm and one neutral density filter with 5% transmissivity. The exposure time was set to 20µs and 35µs for V2 and V5, respectively. The exposure time of V2 at TP04 had to be changed to 25µs, due to lower signal.

2.4.3 Camera setup

Figure 5 shows a sketch of the positioning of the cameras relative to the HOTS. UV-camera and IR-camera are both positioned so that the whole length of the combustor is in the frame. The high horizontal angle-of-view means that the injectors are individually visible in the image. Figure 6 shows the flame fronts of each injector (numerated from 1 to 3). Since the signal of OH*- and H_2O is an integrated quantity along the line-of-sight (LOS), the perceived axial offset of the injectors may lead to misrepresentation of the signal at a given axial position. Nonetheless, the observation and discussion of the LOS-images is done bearing this misrepresentation in mind. The coordinate system departs from the location of injector 1. $x/d_{\mathrm{inj}} = 0$ corresponds to the heat shield location. Accordingly, the discussion about flow field and combustion phenomena in the primary zone is focused on injector 1.

Figure 6 also highlights the presence of reflected UV-signal at the bottom of the combustor, which could not be corrected for. At the same location NIR-signal was reflected towards the IR-camera. Not shown in this figure is the radiation of the hot metal wall-elements in the primary and

mixing zone in the spectrum of the bandpass filter of the IR-camera. This signal contamination depended on the local combustion temperatures and thus on the test point. This error could also not be corrected for.

The interpretation of the OH*- and H_2O-images discussed in Sect. 3 is improved by the addition of characteristic features of the combustor, like injector 1, the mixing rows and the window separators, to the plots.

2.5 Image postprocessing

200 single shot images were recorded by the UV-camera and 400 by the IR-camera. From the raw single shot images an average image was calculated. The average images are normalized by the exposure time used during the recording. This allows for the comparison of the OH*- and H_2O-images between both injectors on the same scale of arbitrary units. A median-filter (5×5 pixel) is applied. Deconvoluted images were extracted from the average images using the python package 'abel' and its 'onion-peeling' method [17]. The deconvolution requires an axisymmetric signal, which can only be assumed for the imaged radiation in the primary zone. However, due to the camera setup the flame images of the presented experiments are not perfectly axisymmetric. This deviation from axisymmetry is expected to affect the interpretation of the flame images negatively regarding location and intensity of the signal. The deconvoluted images can still give qualitative insights into the global structures of the flames when taking this error appropriately into account.

2.6 CFD-data of the flow field

RRD provided the authors with data on the expected flow fields and species concentrations in the primary zone simulated for both injectors using their proprietary CFD-code PRECISE-UNS [18]. RANS-simulations were done for the investigated TPs in the Pearl 15 combustor environment. The Pearl 15 combustor has a similar combustor height and distance between injector and first mixing row. Nonetheless, the combustor liner of Pearl 15 is asymmetric with respect to the injector center line. The simulation was done with $dP_{\mathrm{inj}}/P_{30} \approx 4\%$. The experiments in HOTS at $2\% \leq dP_{\mathrm{inj}}/P_{30} \leq 4\%$ showed no dependence of the location of the flame root on dP_{inj}. Therefore, the CFD-data can be used to comment on the flow field of the experimental flames with $dP_{\mathrm{inj}}/P_{30} = 3\%$. Discrepancies between CFD and the experimental results regarding the location of the heat release were found for the V5-flame. Because of this fact and the slight geometric differences of the combustor only the flow field and mixture fraction near to the injector were used as context for the discussion of the experimental results.

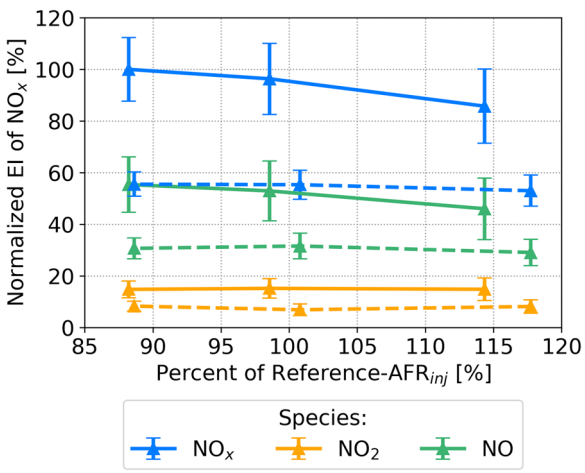

Fig. 7 Emission index of nitric oxides as function of AFR_{inj} at 7% take-off. Markers represent the measured values, which are connected with lines to increase readability. Solid and dashed lines denote injectors V2 and V5, respectively. Error bars show the propagated uncertainty

3 Results and discussion

Figure 7 shows the performance of the investigated injectors regarding their nitric oxides EI. The V5 injector (dashed lines) generates about 55% of the NO_x-emission of V2 (solid lines) at the richer AFR_{inj}. The emissions of the individual nitric oxide species show a similar difference between both injectors. With increasing AFR_{inj} the NO_x-emission of V2 drops by 14% from richer to leaner AFR_{inj}. The respective decrease in NO_x of V5 is lower with just 5%. This points to a relative insensitivity on AFR_{inj} regarding NO_x of V5 compared to V2.

The aim of this section is to discuss two hypotheses explaining the observations regarding the discrepancies in NO_x-performance of both injectors.

> *Hypothesis 1:* The absolute difference in NO_x-emissions can be explained by the disparate flame stabilization location of each flame and the different zonal AFRs
> *Hypothesis 2:* The NO_x-insensitivity of V5 with respect to AFR_{inj} can be explained by increasing heat release in the IRZ with increasing AFR_{inj}.

To corroborate the hypotheses OH*- and H_2O images, coupled with flow field data from the CFD are discussed.

3.1 Flame stabilization and NO_x-formation

The flame stabilization mechanism has a big influence on the driving factors behind final NO_x-emissions, that is T_b, residence time and fuel-air mixture homogeneity. An explanation on the reasons for the different flame stabilization

locations of both injectors may help to understand their influence on NO_x-formation.

Figure 8 shows the deconvoluted flames of V2 and V5 in the primary zone. The limitations of the deconvolution have been explained in Sect. 2.5. Nonetheless big structural differences between V2 and V5 can be observed and cross-examined with the LOS-images. Comparing the heat release zones, marked by OH*-presence near to the injector 1, one can see the distinct flame shapes of both injectors. V2 exhibits an attached flame, while V5 generates a lifted flame in the investigated AFR-range. The lift-off height of the V5-flame is $\frac{1}{3}d_{\mathrm{inj}}$ from the bluff-body. The shapes of the reaction zones close to the injectors, denoted by 'A' in Fig. 8, coincide with the findings of Berger et al. [3] under atmospheric conditions, where a more detailed view and discussion on their shapes at the injector exit over a wider range of AFR is given. The discussion here focuses on the combustion progress from injector to the end of the primary zone upon contact with the first mixing row.

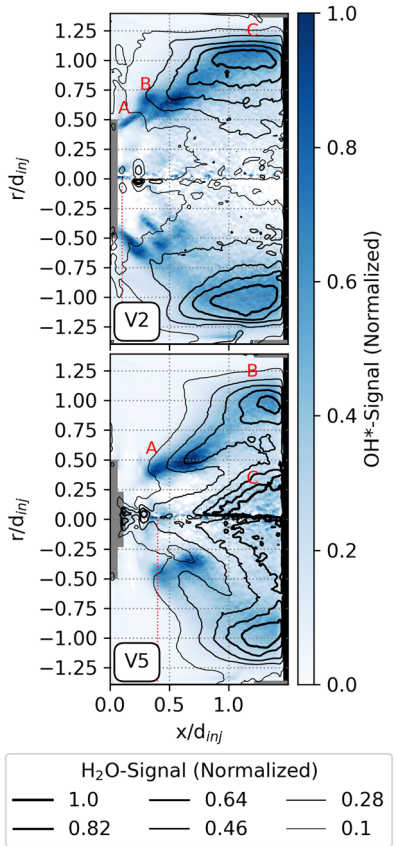

Fig. 8 Upper and lower image show the flame of V2 and V5 at the reference AFR_{inj}. Blue false colors show the deconvoluted OH*-signal. The black lines mark the contour edges of the discretized deconvoluted H_2O-signal. Thicker lines indicate higher H_2O-signal. The counts are normalized by the highest count in the image of the respective injector and species-radiation. The signal of V2 and V5 cannot be compared with each other in absolute terms. The dotted red line shows the position of the signal profile extraction shown in figure 10

Figure 9 shows the size of IRZ of both injectors limited by the $u_x = 0\,m/s$ isoline (extracted from CFD data) closest to the center line. The ORZ is limited by the $ux = 0\,m/s$ isoline in the combustor corners close to the heat shield. V2 has two stoichiometric mixture fraction isolines on either side of the H_2 flow. Flame front A of V2 has been found to correspond to the reaction at the stoichiometric isoline between fuel and inner air flow. The presence of the IRZ suggests transportation of burnt gas into the inner air channel of the injector, where it can mix with the unburnt air. Upon contact of the inner air flow with the hydrogen flow, the conditions for the reaction are given and the flame stabilization is supported by the relatively low axial velocity of the inner air flow. The axial velocity of the inner air flow at the injector exit is half of that of the outer air flow. Flame front B is the result of the reaction of hydrogen with the outer air flow. Figures 8 and 10 show the presence of hot combustion products in the ORZ. The ORZ provides the fuel-air mixture with the necessary activation energy to burn stable. Because of the higher axial velocity of the outer air path (information retrieved from the CFD, but not shown here) this heat release zone stabilizes slightly downstream of the injector. The parallel flow of fuel and outer air flow means that mixing is dominated by turbulence in the shear layer, but will be on a lower level than between fuel flow and swirled inner air flow. This observation leads to the conclusion that the reactions at flame front A and B are well described as non-premixed combustion. Downstream of these distinct heat release zones the fuel reacts continuously with the injector air and with a significant part of the wall cooling air until contact with the first mixing row at location C.

V5 exhibits a lifted flame with the heat release zone at the flame root denoted by 'A'. The reason for this flame stabilization is primarily the central fuel placement and the strong outer air flow. Figure 9 shows that between the two stoichiometric mixture fraction isolines, the fuel-air mixture is rich until the end of the primary zone, including the IRZ. While the IRZ does contain hot burnt gases, as seen in the contour lines of the H_2O-signal in Fig. 8, it is too oxygen-scarce to react with the fuel flow directly downstream of the bluff-body. Similarly, the big ORZ cannot transport radicals and high temperature gases to the location where a combustible fuel-air mixture exists immediately at the exit of the injector, like it is the case for the V2-injector. The stoichiometric mixture fraction isoline is located at the shear layer between the fuel flow and the swirled outer air flow and is shielded by these flows from igniting until the lift-off height is reached. There, enough burnt gas from the IRZ and ORZ have mixed with the fuel and outer air flow to provide the necessary activation energy for the reaction. The design of the intersection of fuel channel and inner air channel additionally impedes any low axial velocity zone, where the flame could stabilize

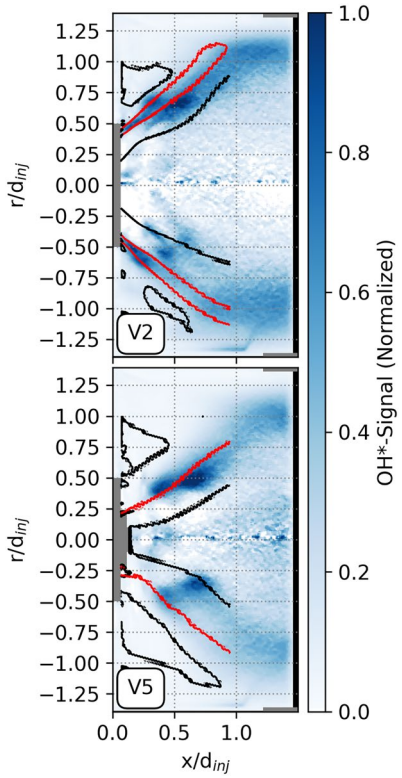

Fig. 9 Upper and lower image show the flame of V2 and V5 at the reference AFR_{inj}. Blue false colors show the deconvoluted OH*-signal. Black lines show the location of u_x = 0 m/s and red lines show the location of the stoichiometric mixture fraction extracted from the CFD

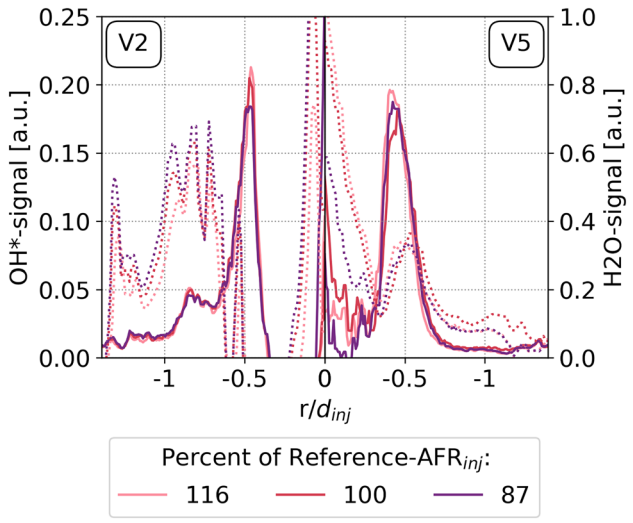

Fig. 10 The left and right plots show the bottom half profiles of V2 and V5, respectively, for the three test points. The profiles are taken at x/d_{inj} = 0.1 for V2 and 0.4 for V5. These positions correspond to the flame roots of both injectors observed in Fig. 8. The signal intensity is plotted on the same scale to allow for quantitative comparison. Solid lines show the deconvoluted OH*-signal profiles. Dotted lines show the deconvoluted H_2O-signal profiles

closer to the injector. The lift-off height allows mixing of fuel and air before reaction and thus the reaction of a more homogeneous fuel-air mixture, which the authors refer to as partially-premixed combustion. Downstream of the heat release zone A the fuel reacts continuously with the injector air and copious amounts of air from heat shield and wall cooling. At location B another OH*-signal peak can be seen presumably where the fuel-rich forward-directed flow from the injector interacts with the first mixing row. Location C, at the end of the IRZ, shows another, less intense, heat release zone, where fuel-rich mixture reacts with either air from the mixing rows or rest air from the forward-directed flow being recirculated into the IRZ.

Figure 10 shows the radial profiles of OH*- and H_2O-signal at the axial location of the flame roots of injector 1 of both configurations. The axial position of the retrieved profiles was determined by matching the OH*-signal peak intensity in the heat release zone A of both injectors. At this axial position disparate H_2O-signal can be observed. The location of the H_2O-signal peaks of both injectors is slightly shifted in radial direction with respect to the OH*-signal peaks. The H_2O-signal peak on the center line of V2 is a reflection on the injector and is ignored. For V2 the highest H_2O-signal is located in the ORZ, while for V5 it is in the IRZ. This is important for the NO_x-formation, since this shows that hot combustion products at the axial location of the flame roots are located in the oxygen-rich ORZ for the V2-injector and in the oxygen-scarce IRZ for the V5.

The different gradients of the OH*-signal around the peak can be explained by the different mixing quality. At the position of the flame root of V2, mixing between fuel and air is limited by the distance to the injector and the fuel and air velocity. The distance from the heat release zone to the injector is much higher for the V5-injector, which leads to a higher degree of mixing. Additionally, the flow field of V5 is such that the inner air flow intersects with the radially redirected swirling fuel flow, which further increases mixture homogeneity at the lift-off height. Therefore, it is expected that the reaction at the flame root of V2 is described well by non-premixed combustion. The reaction of the V5 flame at the lift-off height is expected to be dominated by rich partially-premixed combustion.

The heat release zones at the flame root contribute greatly to the explanation of the absolute NO_x-emission difference between the injectors. The non-premixed combustion of V2 at position A and B lead to high T_b in an oxygen-rich environment (in negative radial direction from the flame front), which leads to high NO_x-formation rates. On the other hand, the rich partially-premixed combustion of V5 at the flame root results in lower T_b and NO_x-production rates, also due to the mixture homogeneity.

The conditions for the formation of NO_x change along the flame front from flame root until contact with the first mixing row. The flow field largely defines the shape of the flame and the amount of air reacting with the fuel. The flow field of both injectors show large differences, of which the recirculation zones have already been discussed above. In Sect. 2.2 the difference of the air split in the combustor due to the difference in effective area of the investigated injectors is explained. Here, the distinct interaction of the fuel-rich flow from the injector with the wall cooling is discussed in further detail.

The V2 image in Fig. 8 shows zones of high intensity OH*-signal being closer to the wall at location C. This observation is underpinned by the big gradient of H_2O-signal perpendicular to the wall, which suggests contact of hot burnt gases with a relatively cold gas flow without water vapour presence, i.e. the wall cooling air. Consequently, it is expected that the fuel-rich mixture downstream of flame fronts A and B partly reacts with fresh air of the wall cooling and heat shield before reaching the first mixing row. Upon reaching the mixing row, hydrogen is strongly depleted. This is due to the relative higher amount of air present in the primary zone, due to the smaller effective area, and the reaction with the wall cooling air. This explains why little to no OH*-signal is seen in the IRZ.

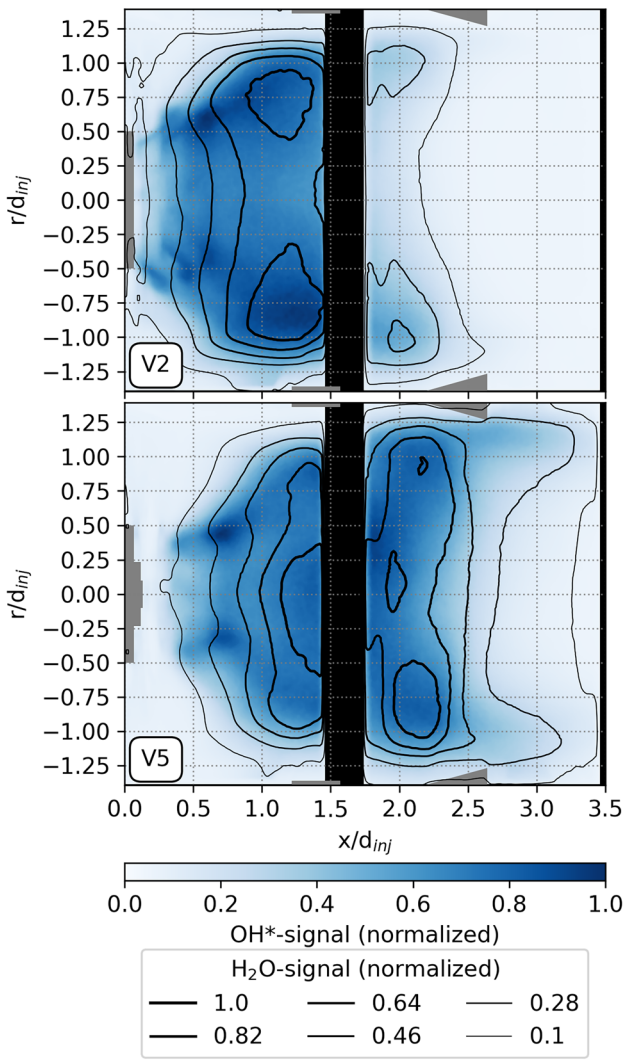

Fig. 11 Upper and lower image show the flame of V2 and V5 at the reference AFR_{inj}. Blue false colors show the OH*-signal. The black lines mark the contour edges of the discretized H_2O-signal. Thicker lines indicate higher H_2O-signal. The counts are normalized by the highest count in the image of the respective injector

In Fig. 11 the reader can see the average LOS OH*-signal being limited to the primary zone with little radiation stemming from the mixing zone. This proves that hydrogen is fully consumed by the end of the primary zone. Since the wall cooling air reacts to a significant extent with the fuel-rich forward-directed flow, the transition from rich to lean combustion takes places before reaching the first mixing row. This results in high T_b being partly recirculated into the IRZ, the tendency of which can be seen in the H_2O-contours bending towards the center line at the end of the primary zone. Hot burnt gases in the oxygen-rich IRZ lead to high NO_x-formation rates and high residence times. This, and the hot combustion products in the ORZ help to understand the high NO_x-emissions from V2 with respect to V5.

At location B in the V5-image in Fig. 8, significant OH*-signal is far away from the wall, at $r/d_{\mathrm{inj}} \approx -0.75$. The gradient of H_2O-signal perpendicular to the wall is much smaller than that for V2. No sudden jump of temperature and water vapour concentration perpendicular to the wall is expected, hinting at a weaker contact of the V5-flame with the wall cooling air. Because the primary zone is globally richer than that of V2 and the hydrogen does not react to the same extent as V2 with the wall cooling and heat shield air, combustion is not limited to the primary zone, but continues into the mixing zone as seen in the average LOS-image of Fig. 11. Unlike the V2-flame, the V5-flame exhibits weak but noticeable OH*-signal in the IRZ at location C accompanied by a large presence of hot burnt gases closer to the injector along the center line. This hints at the presence of combustible air-fuel mixture in the IRZ. The average LOS-image in Fig. 11 also shows a darker spot on the center line at the end of the primary zone of V5. The effect of AFR-variation on this particular heat release zone is discussed further below.

In this regard the V5-configuration acts as a RQL-combustor as intended, where the combustion in the primary zone takes place in the fuel-rich regime, with transition from fuel-rich to -lean happening in the mixing zone with the first and second mixing row.

In summary, the dissimilar homogeneity of the fuel-air mixture at the onset of combustion, leading to different combustion modes, non-premixed vs. partially-premixed,

can help explain the absolute difference in final NO_x-concentration between V2 and V5. The non-premixed combustion regime of V2 at the flame anchoring point leads to high T_b in a region, where on either side of the fuel flow excess air is recirculated towards the flame root. The rich-partially-premixed combustion of V5 at the lift-off height, on the other hand, leads to lower T_b in a fuel-richer environment. The residence times of hot burnt gases downstream of the V2-flame root are higher than those of V5, since the flow velocities are similar, but the distance to the mixing section is longer compared to V5. Furthermore, the different flow fields and different effective areas of both injectors lead to different local stoichiometries in the forward-directed flow between flame root and first mixing row. The local AFR of V2 will be closer to the stoichiometric equivalence ratio before reaching the first mixing row, and thus higher T_b and higher NO_x-production rates are expected than for V5. Burnt gas with higher T_b is then recirculated into the IRZ of V2, where oxygen is present in excess, further enhancing the formation of NO_x. All these differences result in overall higher NO_x EI for V2.

3.2 AFR_{inj} sensitivity of NO_x-Emission Index

The location of the flame root of both injectors remains constant over the AFR_{inj}-range. Coincidentally, the OH*-signal profiles at the axial position of the flame root remains constant. The invariance of the flame stabilization throughout the test points hints at other regions of the combustion to explain the different AFR_{inj} sensitivity of NO_x-emission shown in Fig. 7.

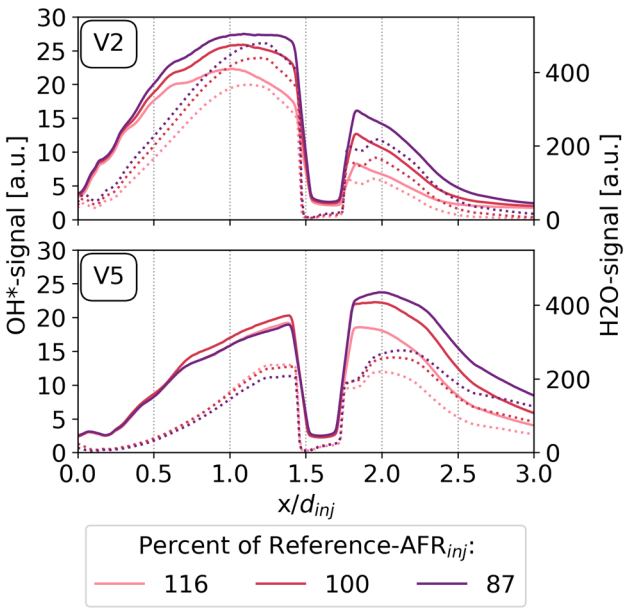

Fig. 12 Upper and lower image show the OH*- and H_2O-signal profiles of V2 and V5 averaged over the height of the combustor for the three investigated AFR_{inj}. Solid lines denote the OH*-signal and dotted lines denote the H_2O-signal

Figure 12 shows the LOS-OH*- and H_2O-signal profiles in axial direction averaged over the combustor height. The steep increase of OH* of the V2-flame up to $x/d_{inj} \approx 0.6$ is the layered effect of heat release zones A and B and the signal of the three injectors overlapping successively. From $x/d_{inj} \approx 0.6$ on the signal increases monotonically and peaks at $x/d_{inj} \approx 1$. The OH*-signal of the richer AFR_{inj} TP plateaus until reaching the mixing zone and then monotonically decreases. The OH*-signal of the reference TP decreases after $x/d_{inj} \approx 1$. The same goes for the leaner TP, but with a higher slope. Decreasing AFR_{inj} does not change the OH*-signal intensity at the axial position of the heat release zones A and B, but it increases the OH*-signal at the axial position of heat release zone C. This fits well with the discussion on the zonal AFRs further above. Decreasing AFR_{inj} means moving the stoichiometric AFR towards the end of the primary zone, that is why the slopes of the signal curves decrease with decreasing AFR_{inj}. The H_2O-signal profile underpins this argument. H_2O-signal peaks at $x/d_{inj} \approx 1.25$ for the reference and richer AFR_{inj} and decreases monotonically after that. The peak is slightly shifted upstream for the leaner TP. Lower AFR means higher absolute heat release, thus higher T_b, and higher water vapour concentration. Higher T_b then leads to higher NO_x-production rates in an oxygen-rich environment. This observation leads to the conclusion that because the flow field and the flame stabilization remain unchanged over the whole AFR-range fuel-air mixture homogeneity stays constant and the residence times change slightly due to changes in the primary zone temperature. T_b, on the other hand, changes significantly with AFR_{inj}.

The behaviour of V5 with respect to changing AFR_{inj} diverges from V2. Figure 12 shows the increase of OH*-signal up to $x/d_{inj} \approx 0.75$ due to heat release zone A and the effect of superimposed signal of the injectors. The average OH*-signal in the primary zone is independent of AFR_{inj}. The H_2O-signal, on the other hand, shows a significant deviation between the richer and leaner TP. The leaner TP leads to higher OH*-signal in the primary zone downstream of heat release zone A.

Figure 13 shows the OH*- and H_2O-signal profiles close to the end of the primary zone. The H_2O-signal of V5 has a peak in the forward-directed flow at $r/d_{inj} \approx -1$. The H_2O-signal at this location is constant for the AFR-variation investigated. Yet, closer to the center line the H_2O-signal becomes dependent on AFR_{inj}. At the center line the signal is still more than half of the peak signal. Similarly, the OH*-signal intensity at the center line is half that of the peak signal. These observations indicate the existence of a heat release zone in the IRZ (in Fig. 8 denoted with C)

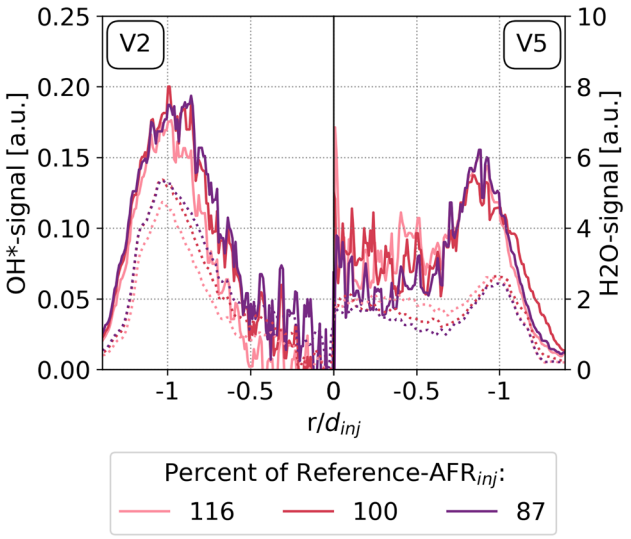

Fig. 13 The left and right plots show the bottom half profiles of V2 and V5, respectively, for the three test points. The profiles are taken at x/d_{inj} = 1.25 for both injectors. The signal intensity is plotted on the same scale to allow for quantitative comparison. Solid lines show the deconvoluted OH*-signal profiles. Dotted lines show the deconvoluted H_2O-signal profiles

and more prominent presence of hot burnt gases in the IRZ with increasing AFR, and thus higher T_b. Going back to Fig. 12, the reader can observe that the richer TP shows higher OH*- and H_2O-signal than the leaner TP in the mixing zone and downstream of it. This behaviour is similar to V2 in the mixing and secondary zone.

The presence of heat release zone C can be explained by the central fuel placement and zonal stoichiometry. Because little of the wall cooling and heat shield air takes part in the combustion, the forward-directed fuel-air mixture is always fuel-rich (as defined by the injector AFR). Consequently, the reaction from injector to first mixing row in the forward-directed flow is limited by the injector air. This explains the relative insensitivity of the OH*- and H_2O-signal at $r/d_{rminj} \approx -1$ seen in Fig. 13, since the investigated AFR's are always fuel-rich. In the IRZ, on the other hand, fresh air from the first mixing row is recirculated towards the injector, mixes with the central fuel flow and reacts. On the center line, in the direction of the injector, this flame front is limited by the hydrogen bubble directly downstream of the bluff-body. As AFR_{inj} decreases the fuel bubble downstream of the bluff-body grows in axial direction, moving the flammable region further downstream. Figure 12 also shows how for the leaner AFR_{inj} the peak H_2O-signal moves from the mixing zone, for the reference AFR and richer AFR, to the end of the primary zone.

In summary, increasing AFR_{inj} leads to higher T_b in the IRZ. While the production rates of NO_x in the forward-directed flow are constant, they increase in the IRZ. Additionally, the IRZ is characterized by longer residence times, which further enhances the final NO_x-emissions stemming from the IRZ. The increasing NO_x-formation rates in the primary zone are compensated by the decrease of T_b downstream of the first mixing row with increasing AFR_{inj}. These disparate contributions to NO_x help explain the seemingly constant emission index of NO_x for the V5 injector in the investigated AFR-range.

4 Conclusion

In the present work two distinct RRD hydrogen injectors, V2 and V5, were tested at engine idle condition. The flames were recorded by imaging the OH*-chemiluminescence and the NIR-radiation of H_2O-molecules. The NO_x-concentration in the exhaust gas was measured as well.

The AFR-variation at 7% take-off load showed the V2-injector emitting significantly more nitric oxides than V5 across all test points. This was found to coincide with the disparate flame stabilization mechanisms and air distribution in the primary zone of the injectors.

V2 exhibits an attached flame governed by non-premixed combustion. This leads to higher flame temperatures in the V2-flame at the first heat release zone and therefore locally higher NO_x production rates. Due to the higher wall cooling mass flow, the transition from fuel-rich to fuel-lean combustion takes place upon contact with the first mixing row. This leads to the highest T_b being found in the primary zone and thus higher NO_x-emissions.

V5 generates a lifted flame with partially-premixed combustion at the flame root. The higher homogeneity of the fuel-air mixture at onset of combustion leads to lower T_b and lower NO_x production rates at the flame root. The transition from fuel-rich to fuel-lean happens in the mixing zone, thus lower T_b in the entirety of the primary zone is expected compared to V2, which leads to lower NO_x-emissions for V5.

The sensitivity of the NO_x-concentration in the exhaust gas on AFR_{inj} was stronger for V2. While EI of NO_x of V2 decreased with increasing AFR_{inj}, it stayed almost constant for V5.

The sensitivity of V2 could be attributed to the location of the heat release zones. By increasing the AFR, the location of the transition from fuel-rich to fuel-lean combustion moves upstream along the forward-directed flow. The average T_b decreases due to the globally leaner combustion, thus reducing NO_x production rates.

The insensitivity of V5 could be attributed to the shift of heat release zones with increasing AFR_{inj}. The forward-directed flow from injector to first mixing row is insensitive to changes of AFR_{inj}. The heat release zone in the IRZ, on the other hand, grows from the end of the primary zone

towards the bluff-body as AFR_{inj} increases. Thus, while NO_x-formation downstream of the primary zone decreases with decreasing AFR_{inj}, the formation of NO_x in the IRZ of the primary zone increases. These counteracting tendencies lead to a seemingly constant NO_x-concentration over the investigated AFR-spectrum.

Few conclusive remarks can be made on the design of hydrogen injectors in RQL-combustors with regard to low NO_x-emissions:

1. The combustion in the primary zone should be designed to be globally fuel-rich with the transition to fuel-lean combustion located in the mixing zone, therefore maximising the effects RQL-technology (as seen with V5)
2. The hydrogen injection design should avoid flame attachment (as seen with V2) on the injector and instead create a lifted flame (as seen with V5) to maximize fuel-air mixing before onset of combustion
3. When using a bluff-body (as in V5), careful consideration should be taken regarding anchoring of hot combustion products, which might damage the injector

The presented investigation added to the literature portfolio of turbulent swirl-stabilized hydrogen flames two application-oriented injectors. Their combustion and emission characteristics have been well understood thanks to the combination of OH*- and H_2O imaging and exhaust gas analysis. To validate the observations made on the changing location of the heat release zone of V5 in it's IRZ, more data from numerical simulations or experimental investigations would be necessary. The gained insights will be of relevance for the design of research-oriented hydrogen and dual-fuel injectors.

Acknowledgements The research leading to these results has received funding from the German Federal Ministry for Economic Affairs and Climate Action (BMWK) in the framework of the LuFo project WOTAN under the grant agreement number (FKZ) 20M2104A and 20M2104B. The authors would like to thank Ruud Eggels of Rolls-Royce Deutschland Ltd. & Co. KG (RRD) for his contribution regarding the CFD-data and the management of RRD for their permission to publish this work. A special thanks is also reserved for the supporting engineers and mechanics who made testing possible.

Author contributions Carsten Clemen, Thomas Behrendt and Sebastián Eisenring conceptualized the test campaign, whereas Carsten Clemen provided the injectors. The original draft was written by Sebastián Eisenring. Measurements were carried out by Sebastián Eisenring and Johannes Berger. Test rig maintenance and operation was supervised and conducted by Peter Tiessen. Measurement data processing was done by Sebastián Eisenring and Johannes Berger. Sebastián Eisenring, Thomas Behrendt, Johannes Berger and Carsten Clemen contributed to the discussion and interpretation. The campaign was supervised by Thomas Behrendt and Bertram Janus. All authors revised the manuscript.

Funding Open Access funding enabled and organized by Projekt DEAL. The research leading to these results has received funding from the German Federal Ministry for Economic Affairs and Climate Action (BMWK) in the framework of the LuFo project WOTAN under the grant agreement numbers (FKZ) 20M2104A (RRD) and 20M2104B (DLR). FKZ-20M2104B was used to finance changes to the test rig infrastructure related to the experiments, while FKZ-20M2104A was used for financing the experiments.

Data availability The authors declare that the data supporting the findings of this study are available within the paper. Additional data sets generated or material collected during the current study are available from the corresponding author upon reasonable request.

Code availability Not applicable.

Declarations

Ethics approval and consent to participate Not applicable.

Conflict of interest The authors declare no conflict of interest.

References

1. Kroniger, D.: Prediction of NOx Emissions for a Hydrogen Fueled Industrial Gas Turbine Combustor with Water Injection (2019). https://doi.org/10.18154/RWTH-2019-02596
2. Giannouloudis, A.: Design, Development and Testing of a High-Pressure Hydrogen Micromix Combustion Rig (2023)
3. Berger, J., Behrendt, T., Eisenring, S., Janus, B., Clemen, C.: Atmospheric Testing of Hydrogen Fuel Injectors for RQL Combustion for the Rolls-Royce Pearl 15 Hydrogen Demonstrator Engine Program. DLRK2024-630106: Submitted to DLRK Congress 2024, Hamburg, Germany
4. Clemen, C., Eggels, R., Gebel, G., Fischer, A., Wurm, B., Staufer, M., Ahrens, D., Lahiri, C.: Development of a Hydrogen Fuel Injector for the Rolls-Royce Pearl 15 Hydrogen Demonstrator Engine Program. DLRK2024-630008: Submitted to DLRK Congress 2024, Hamburg, Germany
5. Lee, D.S., Pitari, G., Grewe, V., Gierens, K., Penner, J.E., Petzold, A., Prather, M.J., Schumann, U., Bais, A., Berntsen, T., Iachetti, D., Lim, L.L., Sausen, R.: Transport impacts on atmosphere and climate: Aviation. Atmos. Environ. **44**(37), 4678–4734 (2010). https://doi.org/10.1016/j.atmosenv.2009.06.005
6. Grewe, V., Matthes, S., Dahlmann, K.: The contribution of aviation NO_x emissions to climate change: Are we ignoring methodological flaws? Environ. Res. Lett. **14**(12), 121003 (2019). https://doi.org/10.1088/1748-9326/ab5dd7

7. Rindlisbacher, T., Ziegler, U.: ICAO Environmental Report: ICAO's work on NOx emissions regulation. https://www.icao.int/sites/default/files/sp-files/environmental-protection/Documents/EnvironmentReport-2010/2025/Envreport2025_13.pdf
8. Lyons, V.: Fuel/Air Nonuniformity - Effect on Nitric Oxide Emissions. In: Proceedings of the Nineteenth Aerospace Sciences Meeting, St. Louis, USA (1981). https://doi.org/10.2514/6.1981-327
9. Hardalupas, Y., Orain, M.: Local measurements of the time-dependent heat release rate and equivalence ratio using chemiluminescent emission from a flame. Combust. Flame **139**(3), 188–207 (2004). https://doi.org/10.1016/j.combustflame.2004.08.003
10. Zhao, M., Buttsworth, D., Choudhury, R.: Experimental and numerical study of oh* chemiluminescence in hydrogen diffusion flames. Combustion and Flame 197, 369–377 (2018) https://doi.org/10.1016/j.combustflame.2018.08.019
11. Kathrotia, T., Fikri, M., Bozkurt, M., Hartmann, M., Riedel, U., Schulz, C.: Study of the h+o+m reaction forming oh∗: Kinetics of oh∗ chemiluminescence in hydrogen combustion systems. Combust. Flame **157**(7), 1261–1273 (2010). https://doi.org/10.1016/j.combustflame.2010.04.003
12. Meier, U., Heinze, J., Magens, E., Schroll, M., Hassa, C., Bake, S., Dörr, T.: Optically Accessible Multisector Combustor: Application and Challenges of Laser Techniques at Realistic Operating Conditions. In: Proceedings of the 2015 ASME Turbo Expo, Montréal, Canada (2015). https://doi.org/10.1115/GT2015-43391
13. BR725: In a class of its own. Accessed: 19.08.2025. https://www.rolls-royce.com/products-and-services/civil-aerospace/business-aviation/br725
14. ECO PHYSICS AG: CLD 700 EL ht: Chemiluminescence Analyzer, Switzerland
15. SICK MAIHAK GmbH: S700 Gas Analyzer: Modular Gas Analyzer System, Germany
16. Rivière, P., Soufiani, A.: Updated band model parameters for h_2o, co_2, ch_4 and co radiation at high temperature. Int. J. Heat Mass Transf. **55**(13–14), 3349–3358 (2012). https://doi.org/10.1016/j.ijheatmasstransfer.2012.03.019
17. Gibson, S., Hickstein, D.D., Yurchak, R., Ryazanov, M., Das, D., Shih, G.: PyAbel/PyAbel: v0.9.0 (v0.9.0) (2022). https://doi.org/10.5281/zenodo.7438595
18. Anand, M.S., Eggels, R., Staufer, M., Zedda, M., Zhu, J.: An advanced unstructured-grid finite-volume design system for gas turbine combustion analysis. ASME 2013 Gas Turbine India Conference (2014) https://doi.org/10.1115/GTINDIA2013-3537